

# TMEM107 recruits ciliopathy proteins to subdomains of the ciliary transition zone and causes Joubert syndrome

Nils J. Lambacher<sup>1,15</sup>, Ange-Line Bruel<sup>2,15</sup>, Teunis J. P. van Dam<sup>3,15</sup>, Katarzyna Szymańska<sup>4</sup>, Gisela G. Slaats<sup>5</sup>, Stefanie Kuhns<sup>1</sup>, Gavin J. McManus<sup>6</sup>, Julie E. Kennedy<sup>1</sup>, Karl Gaffl<sup>1</sup>, Ka Man Wu<sup>5</sup>, Robin van der Lee<sup>3</sup>, Lydie Burglen<sup>7,8</sup>, Diane Doummar<sup>7</sup>, Jean-Baptiste Rivière<sup>2,9</sup>, Laurence Faivre<sup>2,9</sup>, Tania Attié-Bitach<sup>10,11,12,13</sup>, Sophie Saunier<sup>10,11,12</sup>, Alistair Curd<sup>14</sup>, Michelle Peckham<sup>14</sup>, Rachel H. Giles<sup>5</sup>, Colin A. Johnson<sup>4</sup>, Martijn A. Huynen<sup>3,16</sup>, Christel Thauvin-Robinet<sup>2,9,16</sup> and Oliver E. Blacque<sup>1,16</sup>

**The transition zone (TZ) ciliary subcompartment is thought to control cilium composition and signalling by facilitating a protein diffusion barrier at the ciliary base. TZ defects cause ciliopathies such as Meckel–Gruber syndrome (MKS), nephronophthisis (NPHP) and Joubert syndrome<sup>1</sup> (JBTS). However, the molecular composition and mechanisms underpinning TZ organization and barrier regulation are poorly understood. To uncover candidate TZ genes, we employed bioinformatics (coexpression and co-evolution) and identified TMEM107 as a TZ protein mutated in oral–facial–digital syndrome and JBTS patients. Mechanistic studies in *Caenorhabditis elegans* showed that TMEM-107 controls ciliary composition and functions redundantly with NPHP-4 to regulate cilium integrity, TZ docking and assembly of membrane to microtubule Y-link connectors. Furthermore, nematode TMEM-107 occupies an intermediate layer of the TZ-localized MKS module by organizing recruitment of the ciliopathy proteins MKS-1, TMEM-231 (JBTS20) and JBTS-14 (TMEM237). Finally, MKS module membrane proteins are immobile and super-resolution microscopy in worms and mammalian cells reveals periodic localizations within the TZ. This work expands the MKS module of ciliopathy-causing TZ proteins associated with diffusion barrier formation and provides insight into TZ subdomain architecture.**

Cilia are microtubule-based structures serving motility, sensory and signalling functions, and ciliary defects cause broad-spectrum symptoms including cystic kidneys, blindness and nervous system defects<sup>2</sup>. Cilia possess subcompartments with distinct molecular compositions, enriched for receptors, channels and signalling components<sup>3</sup>. Protein targeting to cilia depends on intraflagellar transport (IFT) and membrane trafficking pathways that sort, deliver and recycle ciliary components<sup>4</sup>. A recently established paradigm implicates ‘gated’ diffusion barriers at the ciliary base that regulate protein entry in a size-dependent manner and restrict lateral transport between ciliary and non-ciliary membranes<sup>1,5–10</sup>.

The ciliary gate is associated with the proximal-most 0.2–0.8 μm of the axoneme, termed TZ, characterized by Y-shaped structures that connect the microtubules and membrane. Y-links are also thought to organize the ciliary necklace, a membrane specialization consisting of intramembranous particles that may contribute to diffusion barrier properties<sup>11,12</sup>. Multiple MKS, JBTS and NPHP proteins are TZ-localized and regulate ciliary composition and signalling<sup>5–7,13</sup>. In *C. elegans* sensory neurons, 13 ciliopathy protein orthologues localize at the TZ, where they functionally associate as MKS (MKS-1, MKS-2, MKS-3, MKS-5, MKS-6, MKSR-1, MKSR-2, JBTS-14, TMEM-17, TMEM-231), NPHP (NPHP-1, NPHP-4) or CEP-290-associated modules to regulate Y-link formation and TZ docking during cilium assembly<sup>10,13–19</sup>.

<sup>1</sup>School of Biomolecular and Biomedical Science, UCD Conway Institute, University College Dublin, Belfield, Dublin 4, Ireland. <sup>2</sup>EA4271 GAD, Genetics of Development Abnormalities, Burgundy University, 21078 Dijon, France. <sup>3</sup>Centre for Molecular and Biomolecular Informatics, Radboud Institute for Molecular Life Sciences, Radboud University Medical Center, Geert Grooteplein 26-28, 6525 GA Nijmegen, Netherlands. <sup>4</sup>Section of Ophthalmology and Neurosciences, Leeds Institute of Biomolecular & Clinical Sciences, University of Leeds, Leeds LS9 7TF, UK. <sup>5</sup>Department of Nephrology and Hypertension, University Medical Center Utrecht, 3584 CX Utrecht, The Netherlands. <sup>6</sup>School of Biochemistry and Immunology, Microscopy Facility, Trinity Biomedical Sciences Institute, Trinity College Dublin, 152-160 Pearse Street, Dublin 2, Ireland. <sup>7</sup>Centre de référence des malformations et maladies congénitales du cervelet et Service de Génétique, APHP, Hôpital Trousseau, 75012 Paris, France. <sup>8</sup>INSERM U1141, 75019 Paris, France. <sup>9</sup>FHU TRANSLAD, CHU Dijon, 21079 Dijon, France. <sup>10</sup>INSERM UMR1163, Hôpital Necker-Enfants Malades, 75015 Paris, France. <sup>11</sup>Université Paris Descartes, Sorbonne Paris Cité, 75006 Paris, France. <sup>12</sup>Institut IMAGINE, 75015 Paris, France. <sup>13</sup>Département de Génétique, Hôpital Necker-Enfants Malades, AP-HP, 75015 Paris, France. <sup>14</sup>School of Molecular and Cellular Biology, Faculty of Biological Sciences, University of Leeds, Leeds LS2 9JT, UK. <sup>15</sup>These authors contributed equally to this work.

<sup>16</sup>Correspondence should be addressed to M.A.H., C.T.-R. or O.E.B. (e-mail: martijn.huynen@radboudumc.nl or christel.thauvin@chu-dijon.fr or oliver.blacque@ucd.ie)

To predict new TZ genes, we employed a weighted gene coexpression screening strategy<sup>20</sup>, and a training set of 20 known TZ genes (Supplementary Table 1)<sup>1</sup>, to interrogate >1,600 mouse and human expression microarray data sets in GEO (Supplementary Table 2; top 500 coexpressed genes shown in Supplementary Table 3). In the integrated data sets, TZ genes exhibit higher coexpression with each other than the genomic background (Mann–Whitney *U* tests:  $P = 1.57 \times 10^{-14}$  (human);  $P = 1.42 \times 10^{-9}$  (mouse); Fig. 1a and Supplementary Fig. 1a). Ciliary genes<sup>21</sup> are also enriched (Mann–Whitney *U* tests:  $P = 7.35 \times 10^{-55}$  (human);  $P = 1.43 \times 10^{-44}$  (mouse)), but less than TZ genes (Mann–Whitney *U* tests:  $P = 1.36 \times 10^{-10}$  (human);  $P = 1.01 \times 10^{-6}$  (mouse); Fig. 1a and Supplementary Fig. 1a). Cross-validation (leave-one-out analysis) shows that our method retrieves TZ genes versus ciliary genes, although this is not pronounced among top scoring genes (Fig. 1b).

We compared the top 100 coexpressed human and mouse genes and identified 18 common genes, of which 13 encode proteins with known cilia associations (Supplementary Table 3). For the remaining 5 genes, we examined the genomes of ciliated species lacking a TZ (*Physcomitrella patens*, *Selaginella moellendorffii*, *Plasmodium falciparum* and *Giardia intestinalis*; ref. 22) and found a TZ phylogenetic distribution for *TMEM107* (Supplementary Fig. 1b). Although this gene was previously shown to regulate mammalian ciliogenesis and Shh signalling<sup>23</sup>, the basis of these functions is unknown.

In *C. elegans*, the *TMEM107* orthologue (F39B2.9; *TMEM-107*) is exclusively expressed in ciliated cells and localizes at the TZ (Fig. 1c,d and Supplementary Fig. 2a). Like other TZ genes, worm and human *TMEM107* possess X-box promoter motifs and nematode *tmem-107* expression is exclusively dependent on the RFX transcription factor DAF-19 (Supplementary Fig. 2b,c). *TMEM107* possesses four predicted transmembrane helices and short cytosolic amino and carboxy termini (Supplementary Fig. 1c,d). Disruption of the nematode transmembrane domain linkers or cytosolic N or C termini did not affect localization, suggesting that the TZ association of *TMEM-107* depends on its transmembrane helices (Supplementary Fig. 2d). Similar to *C. elegans* *TMEM-107*, human *TMEM107::GFP* also localizes at the TZ (Fig. 1e).

The TZ localization, combined with reported ciliogenesis and signalling roles<sup>23</sup>, makes *TMEM107* a strong ciliopathy gene candidate. Indeed, similarly to observations for other ciliopathy gene disruptions<sup>24</sup> and the *Tmem107* *Schlei* mouse<sup>23</sup>, *Tmem107*-depleted IMCD3 cells exhibit reduced ciliation and lumen size in three-dimensional spheroids (Fig. 2a,b). To explore disease associations, *TMEM107* exons were screened for mutations in 238 JBTS or oral–facial–digital syndrome (OFD) type VI individuals using Sanger and next-generation sequencing. We identified a homozygous missense variant (NM\_183065: g.8079298T>C; p.Glu45Gly) in OFDVI female twins with consanguineous parents, and a compound heterozygous mutation comprising a frameshift deletion (NM\_032354.3: g.8077560delT; p.Leu134Phe fs\*8) and an in-frame codon deletion (NM\_032354.3: g.8077890\_8077893delGAA; p.Phe106del) in a JBTS male (Fig. 2c and Supplementary Fig. 3a,b). All patients possess similar neurological disturbances, retinopathy and the JBTS-associated molar tooth sign (Fig. 2d–g and Supplementary Fig. 3c). The females were diagnosed with OFDVI because they also exhibit hamartoma and frenulae phenotypes (Supplementary Fig. 3c). All three variants

segregated in the families, were predicted to be pathogenic by Human Splicing Finder and PolyPhen2(p.Phe106del and p.Glu45Gly), and were absent in the heterozygous and homozygous state in human variation databases (NHLBI Exome Variant Server, ExAC). In further support of pathogenicity, fibroblasts from the JBTS male exhibited reduced ciliation, and those cilia that formed were abnormally long (Fig. 2h–j). The latter contrasts with the short cilia of hypomorphic *Schlei* mouse fibroblasts, carrying a missense mutation (E125G) in *Tmem107* (ref. 23); which may be explained by cell type, species or allelic distinctions. We could not use complementation experiments to investigate how the patient mutations affect *TMEM107* function because even moderate *TMEM107*(WT) over-expression was toxic to fibroblast cilium formation. However, *TMEM107*(E45G) and *TMEM107*(F106del) retained the ability to localize at the TZ, indicating that these mutations exert their pathogenicity by disrupting *TMEM107* functions at the TZ, rather than a gross effect on *TMEM107* localizations or stability (Supplementary Fig. 2e).

Next, we investigated the role of *TMEM107* in *C. elegans* TZs. As loss-of-function alleles were unavailable, we used CRISPR-Cas9 (ref. 25) to isolate *oq100*, a 27-base-pair (bp) deletion + 14-bp insertion (Fig. 3a). This mutation causes a frameshift and premature stop, which disrupts transmembrane domains 3 and 4, and is likely to be a null allele as *tmem-107(oq100)::GFP* is not expressed (Fig. 3b). *tmem-107(oq100)* mutants seem normal for dye-filling (indirect measure of cilium integrity<sup>26</sup>), cilium length and morphology, and amphid cilium ultrastructure (Fig. 3c,d and Supplementary Fig. 4a). Also, *tmem-107* mutants possess normal cilia-related chemoattraction and foraging sensory behaviours (Fig. 3e). Thus, *tmem-107* loss does not grossly affect cilium structure and function.

We examined whether *tmem-107* functions redundantly with other TZ genes and found a synthetic genetic interaction with *nphp-4*. Like worms with mutations in a *C. elegans* MKS and an NPHP module gene<sup>10,15</sup>, *tmem-107;nphp-4* double mutants exhibit defects in dye-filling, cilium length and morphology, as well as sensation (Fig. 3c–e). The synthetic cilium structure defects were confirmed by transmission electron microscopy (TEM), which showed that 3–5 amphid pore cilia are truncated or missing in *nphp-4;tmem-107* mutants, whereas most or all axonemes are present in the corresponding single mutants (Supplementary Fig. 4a). Conversely, *tmem-107* does not synthetically interact with *mksr-1* as assessed by dye-filling (Fig. 3c), suggesting that *tmem-107* is part of the MKS module whose genes synthetically interact with NPHP module genes but not with each other<sup>10,15,27</sup>. Importantly, transgenic expression of *tmem-107(WT)::gfp* in *tmem-107;nphp-4* worms rescued the cilium structure and function phenotypes, confirming phenotypic linkage to *oq100* (Fig. 3c,e). Surprisingly, *tmem-107* constructs mimicking the human *TMEM107* patient mutations also rescued the *tmem-107;nphp-4* Dyf phenotype (Supplementary Fig. 4c), and in agreement with these variants retaining functionality, the encoded proteins localized normally (Supplementary Fig. 2d).

TZ ultrastructure was also disrupted in *tmem-107;nphp-4* worms compared with single mutants of *tmem-107* (unaffected) and *nphp-4* (modestly affected; discussed below). In double mutants, Y-links were reduced or missing, and in agreement with loss of these membrane–microtubule connectors, many TZs were undocked from the plasma membrane, frequently extending from ectopic positions within the

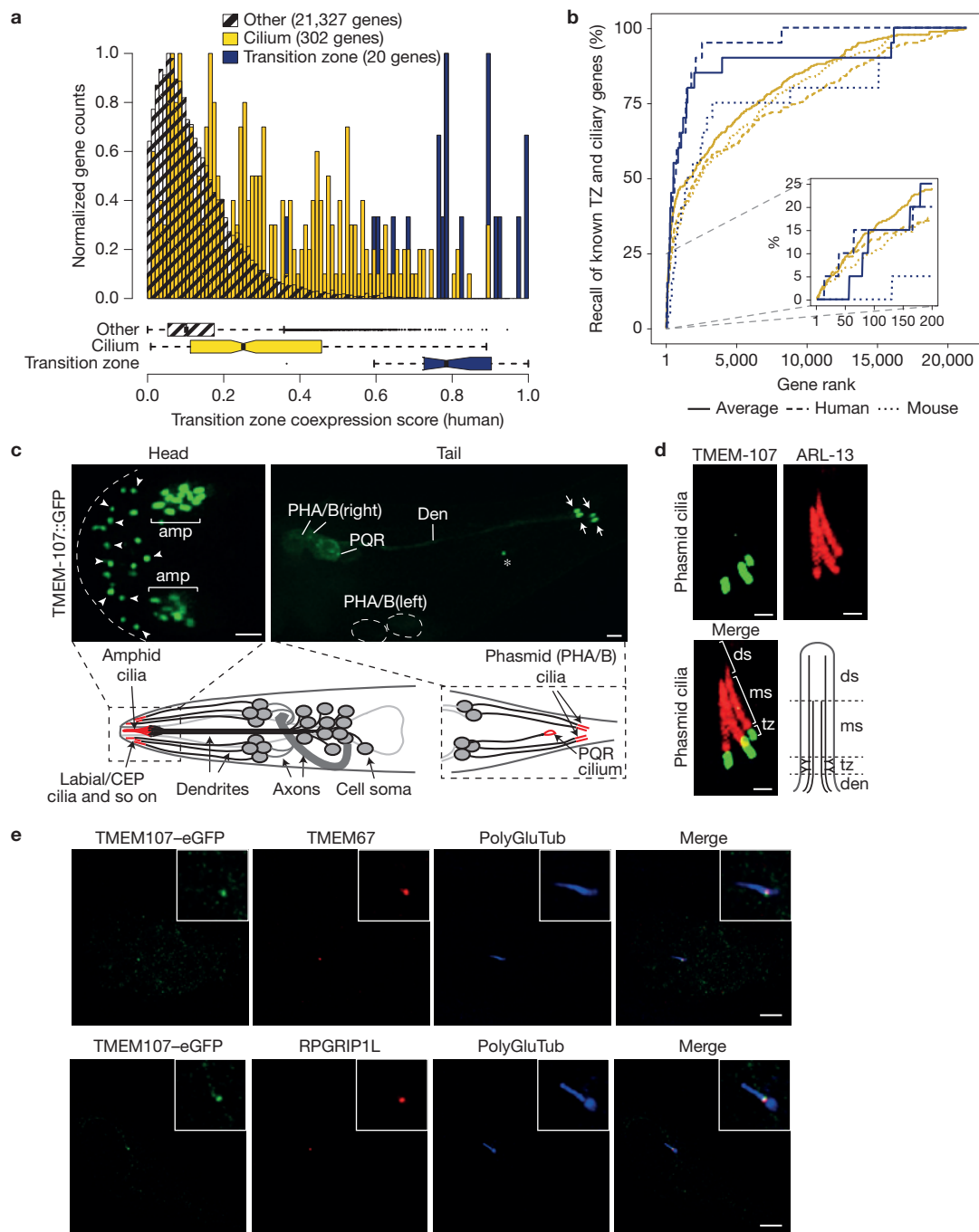


**Figure 1** A weighted coexpression approach to discover TZ genes identifies TMEM107 as a TZ protein. **(a)** Frequency histogram of binned human gene coexpression scores, derived from weighted analyses of gene expression data sets using a training set of 20 known TZ genes (Supplementary Table 1). Frequencies normalized to compare different distributions. SYSCILIA gold standard genes<sup>21</sup> in yellow; TZ gene training in blue; all other genes in grey hatched. Box plots show median and quartiles for histogram distributions. Whiskers (hashed lines) denote the minimum and maximum extent of the data set. **(b)** Recall performance (also known as sensitivity) of the coexpression approach retrieves known TZ (blue lines) and ciliary (yellow lines) genes. The graph shows that TZ genes can be preferentially retrieved compared with ciliary genes. Inset: recall performance for top 200 ranked genes. Ciliary genes taken from the SYSCILIA gold standard<sup>21</sup>. **(c,d)** *C. elegans* TMEM-107::GFP localizes at the TZ. Shown are fluorescence images from worms expressing TMEM-107::GFP alone **(c)** or together with an

ARL-13::tdTomato reporter **(d)**. **(c)** Accumulation of TMEM-107::GFP at the ciliary base region of 12 bilateral amphid cilia (amp; brackets), labial and CEP cilia (subset denoted by arrowheads), bilateral phasmid cilia (arrows) and the right-sided PQR cilium (asterisk) in the tail. Note that the head schematic shows only a subset of the hermaphrodite's ciliated head neurons. **(d)** TMEM-107::GFP localizes immediately proximal to middle segment (ms)-restricted ARL-13::tdTomato. Image shows all four phasmid cilia (left and right). Schematic denotes major subcompartments in phasmid cilia with microtubule doublets (only two shown) in the TZ and middle segments, and microtubule singlets in the distal segment (ds). Den, dendrite. Scale bars, 2  $\mu\text{m}$  (left two images), 1  $\mu\text{m}$  (right images). **(e)** Human TMEM107 localizes at the TZ. Shown are images of hTERT-RPE1 cells stably expressing GFP-tagged human TMEM107 (green) at a low level, co-stained with antibodies for ciliary axonemes (polyglutamylated tubulin, PolyGluTub) and the TZ (RPGRIP1L, TMEM67). Scale bars, 5  $\mu\text{m}$ .

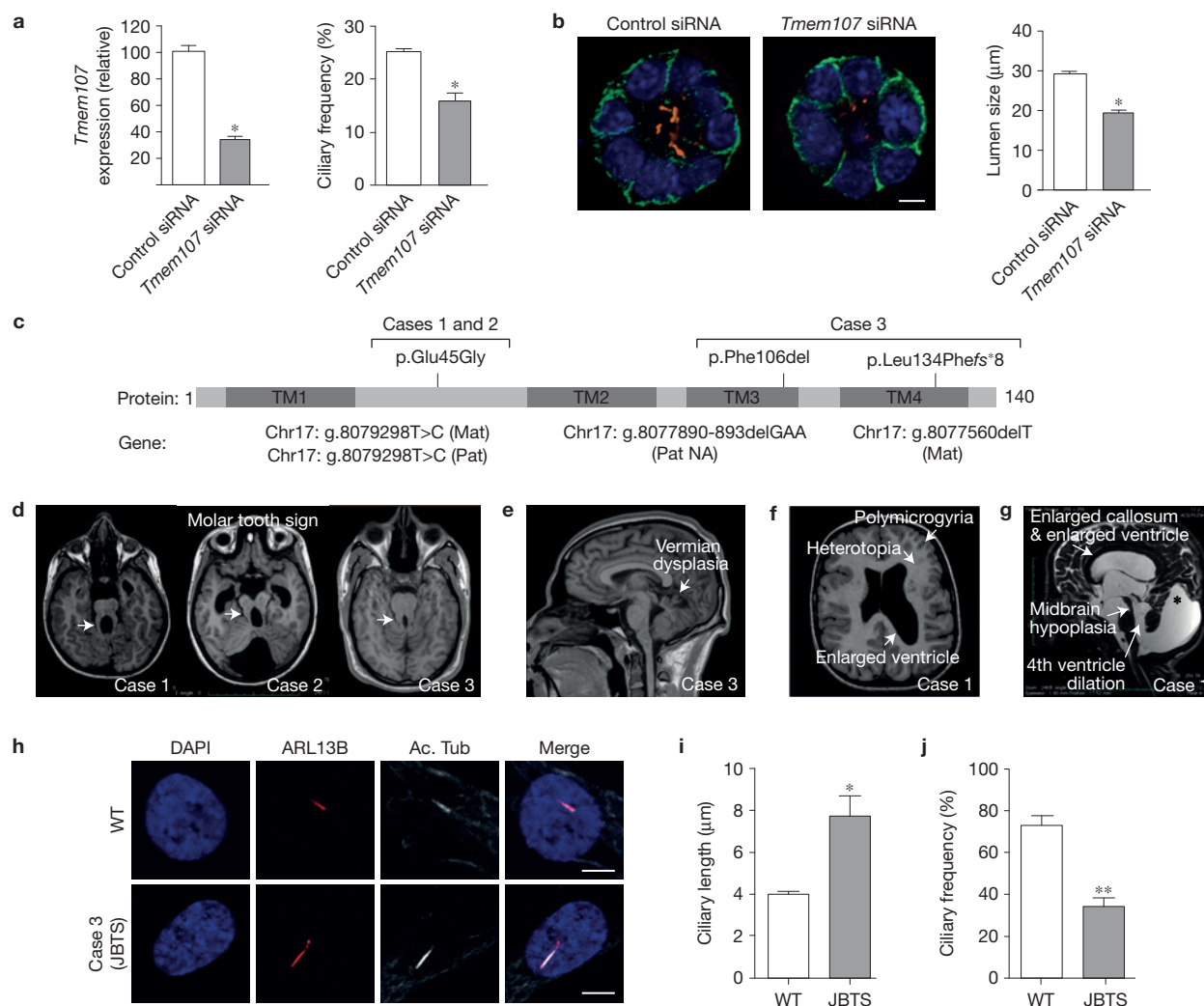


**Figure 2** *TMEM107* regulates mammalian ciliogenesis and is mutated in OFDVI and JBTS individuals. **(a)** IMCD3 cells transfected with *Tmem107* siRNA possess reduced *Tmem107* mRNA expression (versus scrambled siRNA control; qPCR data) and reduced mean ciliary frequency. Data represent mean  $\pm$  s.e.m. ( $n=350$  cells, 1 experiment). \* $P < 0.05$  (unpaired  $t$ -test; versus control). **(b)** When grown in three-dimensional culture, IMCD3 cells transfected with *Tmem107* siRNA form spheroids with a reduced mean size. Cilia (orange) stained for acetylated  $\alpha$ -tubulin; cell junctions (green) stained for beta-catenin. Data represent mean  $\pm$  s.e.m. ( $n=25$  spheroids pooled from 2 independent experiments). \* $P < 0.05$  (unpaired  $t$ -test; versus control). Scale bar,  $5\mu\text{m}$ . **(c)** Schematic of the human *TMEM107* protein showing the position of identified patient mutations. Grey rectangles correspond to the transmembrane domains. Mat, maternal; Pat, paternal; NA, not available. **(d)** Brain magnetic resonance imaging (MRI) images (axial views) showing the molar tooth sign, linked to elongated, thick

and mal-oriented superior peduncles (white arrows) and hypoplastic vermis. **(e)** Brain MRI showing a dysplastic and highly hypoplastic vermis in sagittal view. A secondary enlargement of the fourth ventricle with displacement of the fastigium is also evident. **(f)** Brain MRI (axial view) showing heterotopias, enlarged lateral ventricles and polymicrogyria. **(g)** Brain MRI (sagittal view) showing enlarged posterior fossa (asterisk) with a cystic dilation of the fourth ventricle, a severe midbrain dysplasia and a thin corpus callosum with enlarged ventricles. **(h)** Fibroblasts derived from skin biopsies of healthy control (wild type, WT) and patient 3 (JBTS) immunostained for cilia using antibodies against ARL13B (red; ciliary membrane) and acetylated tubulin (white; axonemal microtubules). **(i, j)** Compared with control cells, JBTS cell cilia possess increased lengths **(i)** and reduced frequencies **(j)**. Data represent mean  $\pm$  s.e.m. ( $n=10$  **(i)** and 25 **(j)** cells; data represent 1 of 3 independent experiments). \* $P < 0.05$ , \*\* $P < 0.01$  (unpaired  $t$ -test; versus WT); scale bars,  $5\mu\text{m}$ .

distal dendrite (Supplementary Fig. 4b). Also, *tmem-107;nphp-4* mutant cilia often exhibited abnormal vesicle accumulations in the TZ and PCMC regions (Supplementary Fig. 4b). Consistent with these structural defects, MKS-2 TZ localization is disrupted in *tmem-107;nphp-4* worms, but not in single mutants (Fig. 3f; *nphp-4* data shown in ref. 15). Furthermore, *tmem-107;nphp-4* neuronal dendrites (phasmids) are frequently short, indicating dendritic tip anchoring defects during dendrite elongation (Fig. 3g)<sup>10,17,27</sup>. Thus, like known MKS module components, *TMEM-107* functionally

interacts with *NPHP-4* to facilitate TZ formation, composition and dendrite formation.

As mentioned above, *nphp-4* single mutants exhibit modest ultrastructural TZ defects, despite previous reports that TZs were normal in these worms<sup>16</sup>. In *nphp-4* worms carrying *tm925* (deletion) or *gk529336* (nonsense) mutations, Y-link densities were frequently reduced and sometimes missing, and undocked TZs were observed in ADF and ADL neurons (Supplementary Fig. 4b). Thus, *C. elegans nphp-4* alone regulates aspects of Y-link assembly or stability, which

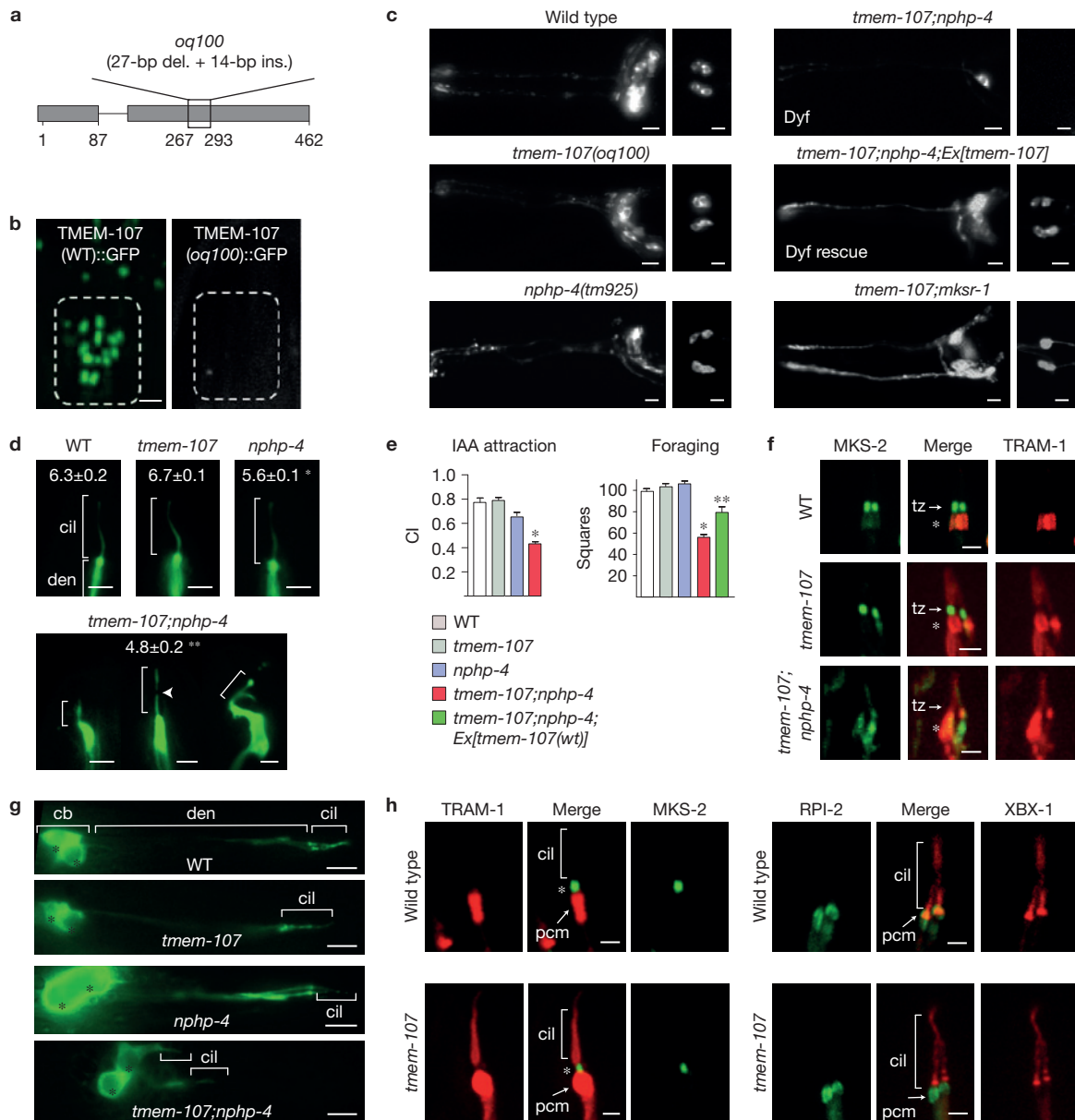


**Figure 3** *C. elegans* *tmem-107* controls diffusion barrier integrity and functions with *nphp-4* to regulate ciliary and TZ structural integrity. (a) Schematic of *oq100* indel mutation in the *tmem-107* gene. Exons denoted by grey rectangles (numbers show nucleotide positions). del., deletion; ins., insertion. (b) *oq100* mutation disrupts TMEM-107 expression. Shown are amphid cilia TZs in worms expressing GFP-tagged wild-type or mutant (*oq100*) TMEM-107. Scale bar, 2  $\mu$ m (images identically scaled). (c) Dye-filling assay (measure of cilium integrity) for 6 amphid (head) and 2 phasid (tail) ciliated neurons showing dye-filling defects (Dyf) in *tmem-107(oq100);nphp-4(tm925)* double mutants, but not single mutants, or a *tmem-107(oq100);mksr-1(tm3083)* double mutant. The Dyf phenotype is rescued by expression of wild-type *tmem-107* (GFP-tagged; see Fig. 1c,d). Scale bars, 10  $\mu$ m. (d) Images of ASER neuronal cilia from worms expressing a *gcy-5p::gfp* that stains the ASER neuron. Numbers refer to cilium length measurements; mean  $\pm$  s.e.m. ( $n=28$  (N2), 44 (*tmem-107*), 46 (*nphp-4*) and 81 (*tmem-107;nphp-4*) cilia). Brackets denote ciliary axonemes (cil). Arrowhead indicates occasional break in GFP staining observed only in double mutant. den; dendrite. \* $P < 0.01$  (unpaired *t*-test; versus WT), \*\* $P = 0.01$  (unpaired *t*-test; versus *nphp-4*); scale bars, 3  $\mu$ m. (e) *tmem-107(oq100);nphp-4(tm925)* double mutants possess defects in cilia-related behaviours. Shown are population assays of isoamyl alcohol (IAA) attraction

and single-worm foraging assays. Data represent mean  $\pm$  s.e.m. For IAA assays,  $n=30$  (N2), 20 (*tmem-107*), 22 (*nphp-4*) and 29 (*tmem-107;nphp-4*); for foraging assays,  $n=44$  (N2), 43 (*tmem-107*), 63 (*nphp-4*), 54 (*tmem-107;nphp-4*) and 37 (*tmem-107;nphp-4;Ex[tmem-107(wt)]*) independent experiments, respectively; \* $P < 0.01$  (unpaired *t*-test; versus WT), \*\* $P < 0.01$  (unpaired *t*-test; versus *tmem-107;nphp-4*). CI, chemotaxis index. (f) TZ composition is altered in *tmem-107(oq100);nphp-4(tm925)* double mutants. Shown are phasid cilia from worms expressing TZ-localized MKS-2::GFP and periciliary membrane-localized, TRAM-1::tdTomato (asterisk). Scale bars, 2  $\mu$ m. (g) *tmem-107(oq100);nphp-4(tm925)* double mutants possess short phasid (PHA/B) dendrites and misplaced cilia. Neurons stained with OSM-6(IFT52)::GFP. cil, ciliary axonemes; den, dendrite; cb, cell bodies (also denoted by asterisks). Brackets denote PHA/B cilia. Scale bars, 5  $\mu$ m. (h) TZ membrane diffusion barrier is selectively disrupted in *tmem-107(oq100)* mutants. Shown are phasid cilia from worms expressing TRAM-1::tdTomato (and MKS-2::GFP; marks TZ) (left images) or RPI-2::GFP (and XBX-1::tdTomato; marks cilia) (right images). TRAM-1 (translocon subunit) and RPI-2 (retinitis pigmentosa 2) are excluded from wild-type (WT) cilia, whereas TRAM-1 (but not RPI-2) leaks into *tmem-107(oq100)* cilia. Asterisk, TZ localization of MKS-2; pcm, periciliary membrane; cil, ciliary axoneme. Scale bars, 2  $\mu$ m.

agrees with the mild cilium structure defects in corresponding mutants<sup>16</sup> (Supplementary Fig. 4a). We conclude that NPHP and MKS modules are not fully redundant in building TZs in at least some amphid channel neurons.

Similar to known MKS module gene mutants<sup>10,15,19</sup>, TRAM-1 abnormally leaks into *tmem-107* mutant cilia, suggesting membrane diffusion barrier defects and altered ciliary composition in these worms (Fig. 3h). However, membrane-associated RPI-2 does not leak into *tmem-107(oq100)* cilia indicating that the barrier is selectively disrupted (Fig. 3h), which contrasts with other MKS module gene mutants, where both TRAM-1 and RPI-2 leak into cilia<sup>10</sup>.

To further investigate TMEM107 associations with MKS module proteins, and the evolutionary conservation of these interactions, three complementary approaches were taken. First, we employed protein localization dependency assays. In *C. elegans*, the MKS module is proposed to assemble hierarchically<sup>10,13,15,19</sup>. In this model, MKS-5 occupies the root of the hierarchy (Layer 1), required for TZ localization of all MKS module components. In contrast, MKS-3, JBTS-14, MKS-6 and TMEM-17 occupy a peripheral level (Layer 3) not required for localization of other proteins, whereas MKSR-1, MKSR-2, TMEM-231 and MKS-2 form an intermediate level (Layer 2), required for Layer 3 but not Layer 1 protein targeting. To evaluate whether TMEM-107 is part of this model, TMEM-107::GFP localization was assessed in MKS module gene mutants, and MKS module protein localizations were analysed in *tmem-107(oq100)* mutants. We found that TMEM-107 is not required for Layer 1 and most Layer 2 protein localizations, but is required for the organization of Layer 3 proteins (JBTS-14, TMEM-17), as well as MKS-1 (unassigned layer) and TMEM-231 (layer 2) (Fig. 4a). In reverse experiments, TMEM-107 localization depends on Layer 1, 2 and MKS-1 proteins, but not Layer 3 proteins (Fig. 4a). Furthermore, TMEM-107 and NPHP module proteins are not localization interdependent (Fig. 4a). These data show that TMEM-107 recruits an MKS submodule of proteins (TMEM-17, TMEM-231, JBTS-14, MKS-1) and suggest that TMEM-107 occupies an intermediate layer, connecting Layer 2 to a Layer 3 subset (Fig. 4b). Interestingly, TZ recruitment of TMEM-17 and TMEM-231 by TMEM-107 is independent of its short cytosolic N and C termini, suggesting that this function is orchestrated by the transmembrane helices or interhelical linkers (Fig. 4c). In agreement with our nematode data, depletion of mammalian *Tmem107* also alters the localization of some MKS module proteins (Tmem231 and Tmem237) but not others (Rpgrip1l; Fig. 4d).

In the second approach, co-immunoprecipitation (coIP) assays were performed to determine whether mammalian TMEM107 biochemically associates with MKS module proteins. GFP-tagged TMEM107 was exogenously coexpressed with FLAG-tagged TMEM216, TMEM231, TMEM17 or TMEM237, or with myc-tagged MKS1, and assessed for associations in IMCD3 cells using binding conditions optimized for membrane proteins<sup>28</sup>. We found that TMEM107 immunoprecipitates full-length TMEM216, TMEM231, TMEM237 and MKS1, but not TMEM17 (Fig. 4e). For TMEM237, TMEM107 did not detectably interact with an N-terminal cytoplasmic domain of this protein (TMEM237Nt), indicating that the TMEM237 association depends on its transmembrane helices or C-terminal cytoplasmic domain (Fig. 4e).

In the third approach, we used differential Dollo parsimony<sup>29</sup> to obtain co-evolutionary relationships for MKS module proteins.

In agreement with the nematode hierarchy<sup>10,15</sup>, Layer 2 orthologues TMEM216, B9D1 and B9D2 form a co-evolving MKS core (Fig. 4f). This 'core' co-evolves with Layer 3 orthologues TMEM67 and CC2D2A, consistent with localization dependencies in mammalian systems<sup>5</sup>, although not in worms (Fig. 4f). We also identified a co-evolving TMEM107, TMEM17 and TMEM231 submodule, again agreeing with nematode localization dependencies (Fig. 4f). Unexpectedly, this submodule does not include TMEM237 because orthologues are missing in stramenopiles, alveolates and excavates (Supplementary Fig. 1b), indicating late incorporation into the MKS module. Also surprising was that RPGRIP1L only marginally co-evolves with the MKS module, despite its central role in module organization<sup>10,19</sup> (Fig. 4f). This may be explained by low RPGRIP1L sequence conservation and difficulties in assigning orthologues. Finally, the interdependent MKS1 and TMEM107 localizations are not reflected in the co-evolution data. Thus, our evolutionary findings support conserved roles for *C. elegans* TMEM-107 in organizing an MKS submodule with TMEM-231 and TMEM-17, but differences in the modular arrangements of TMEM-107 with other MKS proteins might exist between species.

The specific TZ localization of MKS module proteins, together with their requirement for Y-link assembly with NPHP proteins, could suggest that this module interacts with Y-links or associated structures. If true, MKS module proteins should be immobile. Using fluorescence recovery after photobleaching (FRAP) assays in *C. elegans*, photobleaching one half of the TZ signal for TMEM-107::GFP, MKS-2::GFP and MKS-6::GFP resulted in no signal recovery (30 min), indicating that the non-bleached TZ pool is immobile (Fig. 5a). Also, no recovery was observed when entire TZ signals were photobleached (MKS-2::GFP), demonstrating that MKS module proteins possess slow TZ entry kinetics (Supplementary Fig. 5a). This immobility depends on other MKS module proteins because MKS-2 is highly mobile in *mksr-1* (B9D1) mutants (Fig. 5b). Therefore, we conclude that transmembrane (TMEM-107, MKS-2) and membrane-associated (MKS-6) proteins are anchored at the TZ membrane. Furthermore, at least for MKS-2, anchoring requires an intact MKS module.

Next, we used stimulated emission depletion (STED) super-resolution microscopy to further investigate *C. elegans* MKS (TMEM-107, MKS-2 and TMEM-231) and NPHP (NPHP-1) module protein distributions within TZs. Side-view TZ images (axial orientation) revealed that these proteins are periodically distributed along the axial plane, frequently appearing as multiple independent rings (partial or complete), or possibly spiral structures (Fig. 5c and Supplementary Fig. 5b). However, in some images with slightly better resolution, individual dots of signal were evident within ring-like domains (Fig. 5c; arrowheads), suggesting that these domains consist of multiple discrete protein clusters. Punctate signals were also observed for NPHP-1, suggesting that MKS and NPHP module proteins possess similar axial TZ distributions (Fig. 5c). We were unable to determine protein distributions from true transverse (radial) views of the TZ because of the orientation of worms (and cilia) on the imaging slide.

We also performed STED imaging on endogenous RPGRIP1L and TMEM67 in human cells (RPTEC-TERT1). Imaging of TZs in the radial orientation revealed that these proteins can form discrete clusters arranged as a complete or near-complete single shallow ring (Fig. 5d and Supplementary Fig. 5c). Although the number of resolved

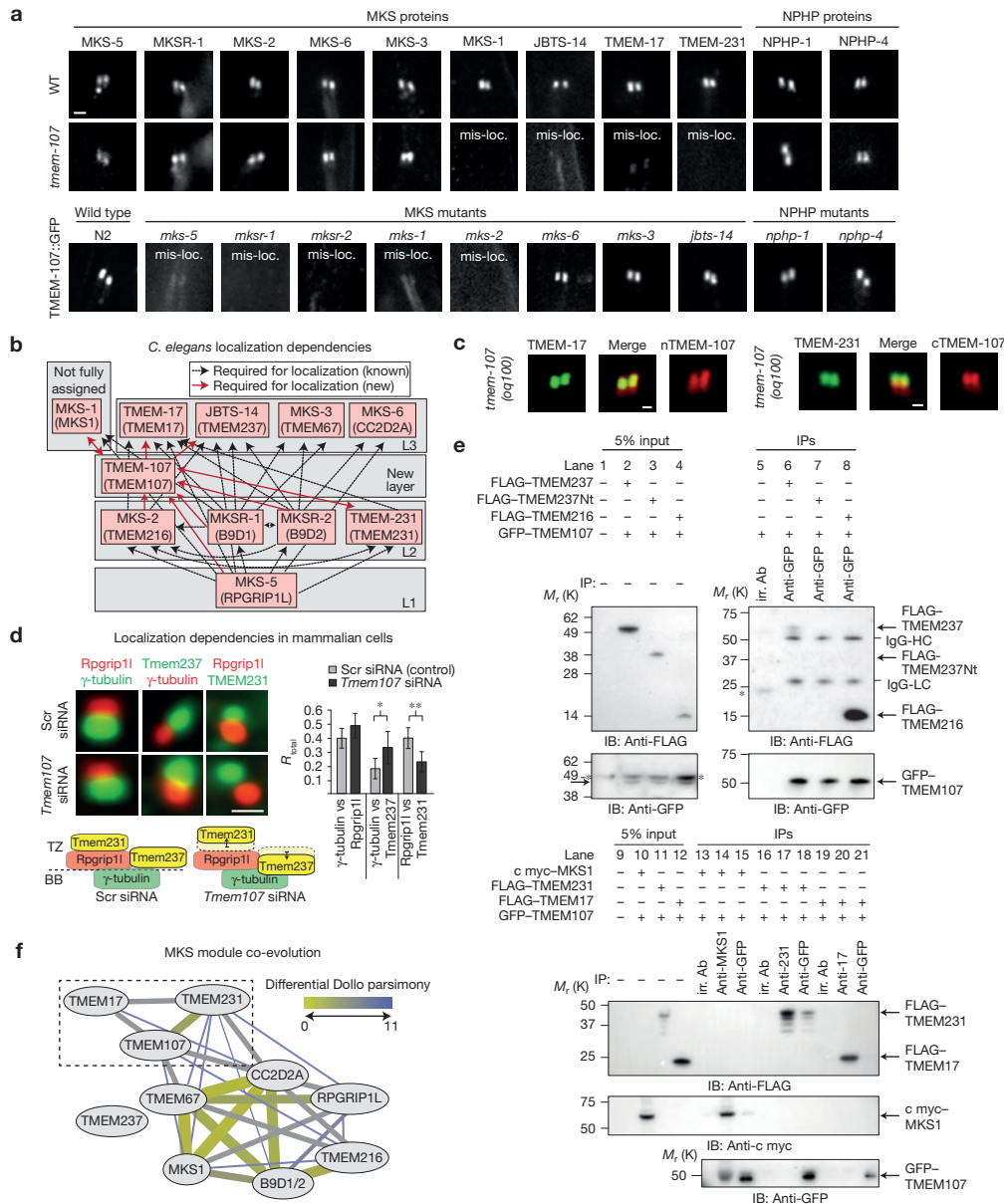


**Figure 4** Evolutionarily conserved association of TMEM107 with the TZ-localized MKS module. **(a)** Phasmid TZ localizations of GFP-tagged MKS and NPHP module proteins in WT and *tmem-107(oq100)* mutant worms, and TMEM-107::GFP in MKS and NPHP mutants. Scale bar, 1  $\mu$ m (all images similarly scaled). mis-loc., mislocalized. **(b)** Schematic summarizing TZ localization dependencies in **a**. TMEM-107 positioned at an intermediate level within a hierarchical three-layer (L1-3) MKS module assembly model (drawn on the basis of refs 10,13,15,19; MKS-1 'unassigned' because hierarchical analysis has not yet been conducted using an *mks-1* null allele). Human orthologues denoted in brackets. **(c)** Expression of TMEM-107::RFP with disrupted cytosolic N or C termini (nTMEM-107, cTMEM-107; see Methods) rescues mislocalized TMEM-17::GFP and TMEM-231::GFP in *tmem-107(oq100)* mutants. Shown are phasmid cilia TZs. Scale bars, 0.5  $\mu$ m. **(d)** *Tmem107* depletion (siRNA) in IMCD3 cells disrupts relative localizations of endogenous MKS module proteins. Cells double-stained as indicated and co-localization determined as an  $R_{total}$  Pearson correlation value (FIJI 'Co-localization Threshold' plug-in). In *Tmem107*-depleted cells, Rpprip11 localization is unaffected (relative to basal body (BB)  $\gamma$ -tubulin), whereas Tmem231 and Tmem237 proteins shift (black arrows) relative to  $\gamma$ -tubulin or Rpprip11. Data in graph represent mean  $\pm$  s.e.m. ( $n=150$  cells pooled from 3 independent

experiments). Scr siRNA, siRNA scrambled control.  $**P < 0.01$ ,  $*P < 0.05$  (unpaired *t*-test; versus Scr siRNA control). Scale bar, 1  $\mu$ m. **(e)** Co-immunoprecipitation (coIP) assays in IMCD3 cells. Upper panels, lanes 1-4: input material from whole cell extracts (WCEs) transfected with the indicated constructs and immunoblotted (IB) with anti-GFP or anti-FLAG. Lanes 5-8: proteins immunoprecipitated (IP) by an irrelevant antibody (irr. Ab; anti-MICU3) or anti-GFP, and then immunoblotted for FLAG or GFP. IgG heavy chain (HC) and light chain (LC) in co-immunoprecipitates are indicated. Asterisks (\*) mark nonspecific proteins. Lower panels, lanes 9-12: input WCE showing expression of FLAG-TMEM231, FLAG-TMEM17 and c myc-MKS1. Lanes 13-21: IPs with antibodies against MKS1 (lane 14), TMEM231 (231; lane 17) and TMEM17 (17; lane 20) and then immunoblotted as indicated. Note that although TMEM107 co-immunoprecipitates TMEM231, TMEM231 does not co-immunoprecipitate detectable levels of TMEM107. Unprocessed original scans of blots are shown in Supplementary Fig. 6. **(f)** Co-evolution relationships between MKS components using differential Dollo parsimony that counts along a phylogenetic tree how often two genes are lost independently from each other. Thickness and colour gradient indicate strong co-evolution. Edges with differential Dollo parsimony scores  $>11$  are not shown. Dashed rectangle: co-evolving MKS submodule.

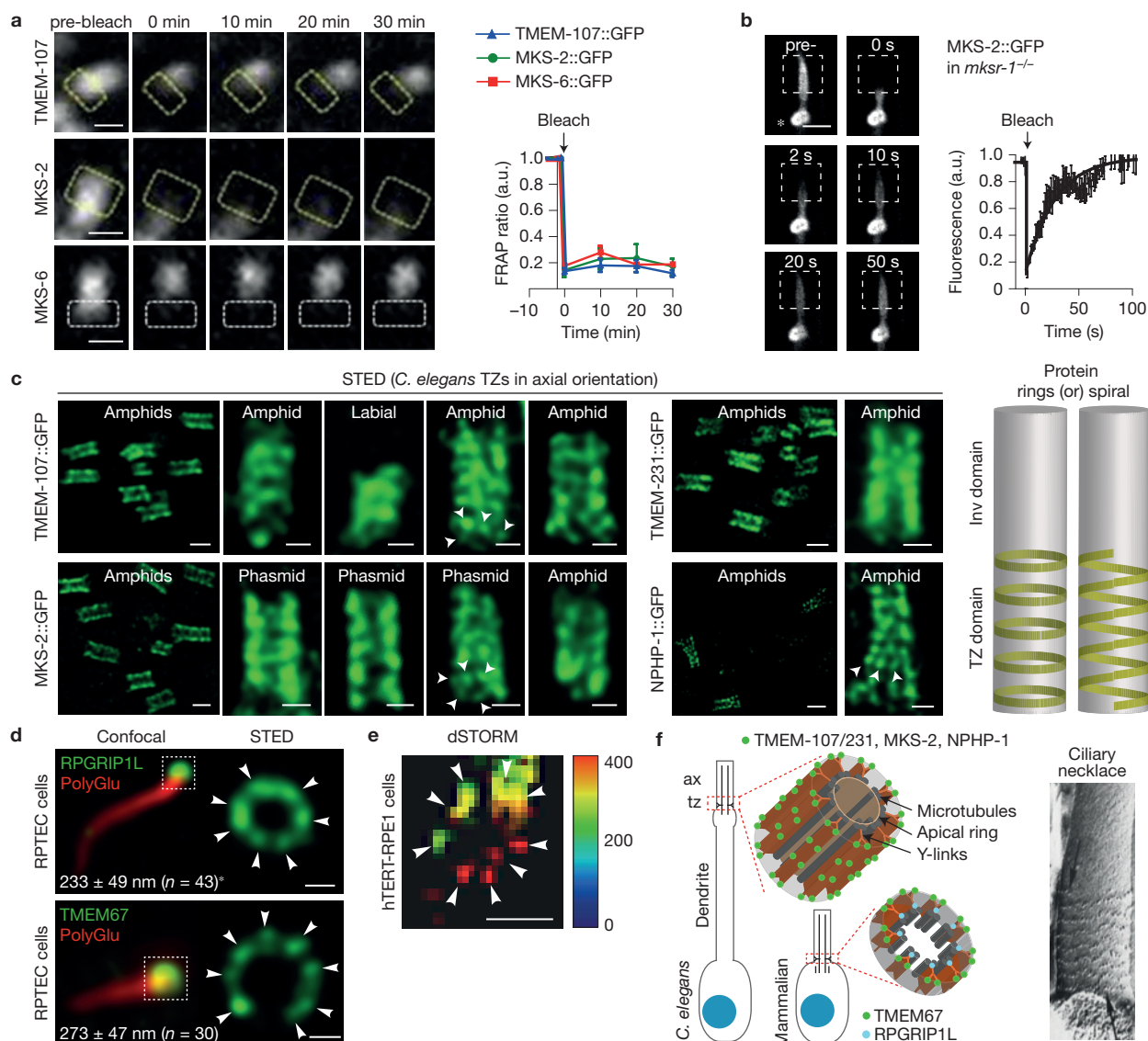


**Figure 5** Anchoring and periodic distributions of MKS module proteins within the TZ. (a) GFP-tagged TMEM-107, MKS-2 and MKS-6 are immobile within the *C. elegans* TZ. Shown are FRAP curves and representative time-lapse images after photobleaching one half of a TZ signal (outlined region). Data points represented as mean  $\pm$  s.e.m. ( $n=3$  (MKS-6) or 4 (TMEM-107, MKS-2) independent experiments). Scale bars, 500 nm. (b) *C. elegans* MKS-2 immobility depends on MKS module proteins. Shown is a FRAP curve and representative time-lapse images (phasmid cilia) after photobleaching MKS-2::GFP signals (boxed region) in an *mksr-1* mutant. Asterisk, periciliary membrane. Data points represented as mean  $\pm$  s.e.m. ( $n=4$  independent experiments). a.u., arbitrary units; scale bar, 2  $\mu$ m. (c) STED super-resolution microscopy images of *C. elegans* MKS and NPHP module protein (all GFP-tagged) distributions in transition zones. Shown are single focal plane images of TZs in axial orientation (from the side) taken from head (amphid, labial) and tail (phasmid) ciliated neurons. Note the smaller size of the labial cilium TZ. Schematics indicate ring-like or spiral-like domains formed by the *C. elegans* MKS/NPHP module proteins. Arrowheads show independent signal clusters within a ring-like domain. Scale bars, 200 nm (high-magnification images), 500 nm (low-magnification images). (d) STED images of endogenous human

RPGRIP1L and TMEM67 in renal RPTEC cells showing clusters (arrowheads) of protein in a single ring of differing diameters (mean  $\pm$  s.d.) at the TZ. Corresponding confocal images co-stained for cilia with polyglutamylated tubulin antibody. \* $P=0.001$  (unpaired *t*-test; versus TMEM67). Scale bars, 100 nm. (e) dSTORM of human RPGRIP1L (visualized with Alexa Fluor 647) with 10 nm binning, image smoothing and contrast enhancement in FIJI (raw images shown in Supplementary Fig. 5d), showing periodic localization (arrowheads) in a loose ring at the TZ. Image depth-coded by colour. Z-axis scale bar (nm) on right. Scale bar, 100 nm. (f) Models. MKS module proteins (and *C. elegans* NPHP-1) occupy periodic radial and axial TZ subdomains. Mammalian RPGRIP1L and TMEM67 localize as independent clusters, forming a single ring domain at the TZ core (RPGRIP1L) or membrane (TMEM67). *C. elegans* MKS and NPHP proteins also localize as discrete independent clusters, forming multiple ring domains (or possible spiral domains) along the TZ length. The nematode axial distribution may correspond to the ciliary necklace (TEM example from ref. 12). Periodicity and immobility of MKS module proteins suggests association with Y-links, which form extended sheets in *C. elegans* (Supplementary Video 1) and are implicated in necklace formation.

clusters was variable, rings with 7–8, or possibly 9 clusters were observed. In addition, RPGRIP1L ring diameters were significantly narrower than TMEM67 ring diameters (Fig. 5d). As an alternative

approach, we imaged endogenous RPGRIP1L using direct stochastic optical reconstruction microscopy (dSTORM). Similar to our STED findings, dSTORM imaging of RPGRIP1L revealed a single shallow

ring of TZ signal, comprised of at least 7–8 independent puncta (Fig. 5e and Supplementary Fig. 5d). Thus, both mammalian RPGRIP1L and TMEM67 seem to be organized as discrete clusters within ring-like domains of differing diameters, indicating distinct radial positioning at the TZ membrane (TMEM67) and core (RPGRIP1L). The periodicity of these clusters approaches the nine-fold symmetry of Y-links, suggesting possible association with these structures.

Our super-resolution imaging indicates that MKS module proteins occupy periodic radial and axial subdomains of the TZ core and membrane (Fig. 5f). The nematode axial pattern is reminiscent of the ciliary necklace, a conserved TZ membrane specialization comprised of 1–7 rows of intramembrane leaflet particles identified over 40 years ago<sup>11,12</sup> (Fig. 5f). In further support of a necklace association, *C. elegans* MKS module proteins are anchored at the TZ membrane, and the periodic radial distribution of mammalian TMEM67 at the TZ membrane approaches the periodicity of Y-links implicated in necklace formation<sup>11</sup>. In one model, Y-links would anchor MKS module proteins at the necklace (Fig. 5f). However, a tomographic (TEM) reconstruction of a portion of the *C. elegans* TZ indicates that Y-links are continuous structures running the TZ length (Supplementary Video 1 and Fig. 5f; see also ref. 18); thus, any association of MKS proteins with Y-links would occur at various axial positions along continuous Y-link sheets (Fig. 5f). Unfortunately, we could not identify a necklace pattern for mammalian MKS module proteins because of spatial constraints and resolution limits conferred by the short TZ (<200 nm). Future super-resolution imaging on mammalian cells with longer TZs should clarify the nematode observations.

In summary, we have identified TMEM107 as a ciliopathy TZ protein and conserved MKS module component. Causality of the mutations identified here to JBTS and OFDVI is supported by very recent reports of additional *TMEM107* mutations linked to MKS and OFD (refs 30,31). Furthermore, we show that ciliopathy proteins are anchored at the TZ membrane, and exhibit periodic radial and axial distributions at the TZ core and membrane. In addition, our finding that MKS-2 is mobile in *mksr-1* (B9D1) mutant cilia indicates that protein anchoring at the TZ is important for barrier functions. Strikingly, membrane diffusion barriers of the axon initial segment (AIS) that limit free exchange of phospholipids also depend on anchored membrane proteins<sup>32</sup>, and sodium channels within the AIS membrane are coordinately localized with evenly spaced (180–190 nm) actin–spectrin cytoskeletal rings<sup>33</sup>. Thus, the TZ and AIS cellular compartments may share comparable molecular organization underpinning common mechanisms of barrier function. Finally, our bioinformatics analysis to discover genes of the TZ compartment goes beyond most comparative genomics studies that focus on the entire cilium. Indeed, distinct phylogenetic signatures exist for other ciliary modules such as IFT-A, IFT-B and BBSome assemblies<sup>34</sup>. Thus, exploitation of genomics data can help to disentangle ciliary modules, ultimately leading to a greater understanding of ciliary transport, signalling and disease. □

## METHODS

Methods and any associated references are available in the [online version of the paper](#).

Note: Supplementary Information is available in the [online version of the paper](#)

## ACKNOWLEDGEMENTS

This work was financially supported via the European Community's Seventh Framework Programme FP7/2009 (SYSCILIA grant agreement 241955 to O.E.B., M.A.H., R.H.G. and C.A.J.), and Gencodys to M.A.H.), Science Foundation Ireland (11/PI/1037 to O.E.B.), the Dutch Kidney Foundation CP11.18 'KOUNCIL' (to R.H.G.), the GIS-Institut des Maladies Rares (HTS to C.T.-R.), the French Fondation for Rare Disease (to C.T.-R.), the Virgo consortium (FES0908 to M.A.H.), the Netherlands Genomics Initiative (050-060-452, RvdL to M.A.H.), the French Ministry of Health (PHRC national 2010-A01014-35 and 2013 to C.T.-R.), the Fondation pour la Recherche Médicale (DEQ20130326532 to S.S.), the Regional Council of Burgundy (to C.T.-R.), a Sir Jules Thorn Award for Biomedical Research (JTA/09 to C.A.J.), and the UK Medical Research Council (MR/K011154/1 to C.A.J., and MR/K015613/1 to M.P.). We thank the patients and their families for their participation. We also thank the NHLBI GO Exome Sequencing Project and its ongoing studies that produced and provided exome variant calls for comparison: the Lung GO Sequencing Project (HL-102923), the WHI Sequencing Project (HL-102924), the Broad GO Sequencing Project (HL-102925), the Seattle GO Sequencing Project (HL-102926) and the Heart GO Sequencing Project (HL-103010). We thank M. Leroux (Simon Fraser University, Canada), B. Yoder (University of Alabama, USA), the *Caenorhabditis elegans* Genetics Center (Minnesota, USA), the National Bioresource project (Tokyo, Japan), the International *C. elegans* gene knockout consortium, and the *C. elegans* Million Mutation Project for nematode reagents. We are grateful to C. Eggeling and C. Lagerholm (Weatherall Institute of Molecular Medicine and the Wolfson Imaging Center, Oxford, UK) for assistance with STED microscopy, D. Scholz and T. Toivonen (UCD Conway Institute imaging facility, Dublin, IRL) for imaging support, and R. Dijkstra (Scientific Volume Imaging bv, Hilversum, NL) for assistance with STED image deconvolution. We also thank A. Cleasby (Faculty of Biological Sciences, University of Leeds, Leeds, UK) for help with developing the dSTORM technique, B. Chih (Genentech, South San Francisco, CA, USA) for the kind gift of polyclonal anti-TMEM17 and TMEM231 antibodies, and T. McMorro (University College Dublin, Dublin, Ireland) for the generous gift of the RPTEC/TERT1 cells. We thank D. Rodriguez (Trousseau hospital, Paris) for assistance with analysis of brain MRIs. The dSTORM microscope was generously funded by alumnus M. Beverly, in support of the University of Leeds 'making a world of difference campaign'.

## AUTHOR CONTRIBUTIONS

N.J.L., J.E.K., K.G. and O.E.B. performed and interpreted experiments with *C. elegans*. T.J.P.v.D., R.v.d.L. and M.A.H. performed all bioinformatics analyses. A.-L.B., L.B., D.D., T.A.-B., S.S. and C.T.-R. collected and purified patient samples, performed exome sequencing and analysed sequencing data. N.J.L., S.K. and G.J.M. performed the STED imaging. A.C., M.P. and C.A.J. conducted the dSTORM imaging and processing. K.S., S.K., G.G.S., K.M.W. and R.H.G. conducted transfection and immunofluorescence microscopy in mammalian cells. K.S. and C.A.J. contributed the co-immunoprecipitation experiments. J.-B.R., L.F. and C.T.-R. diagnosed and referred patients. The co-corresponding authors shared supervision of the work. M.A.H. uncovered TMEM107 as a candidate ciliary gene, and directed the bioinformatics work. C.T.-R. collated JBTS and OFD patient samples, performed clinical characterization and directed the sequencing. O.E.B. directed research, analysed and collated data for the manuscript. O.E.B., M.A.H., R.H.G. and C.A.J. conceived and executed the study, and O.E.B., N.J.L., T.J.P.v.D. and M.A.H. wrote the manuscript.

## COMPETING FINANCIAL INTERESTS

The authors declare no competing financial interests.

Published online at <http://dx.doi.org/10.1038/ncb3273>

Reprints and permissions information is available online at [www.nature.com/reprints](http://www.nature.com/reprints)

- Reiter, J., Blacque, O. & Leroux, M. The base of the cilium: roles for transition fibres and the transition zone in ciliary formation, maintenance and compartmentalization. *EMBO Rep.* **13**, 608–618 (2012).
- Goetz, S. C. & Anderson, K. V. The primary cilium: a signalling centre during vertebrate development. *Nat. Rev. Genet.* **11**, 331–344 (2010).
- Blacque, O. E. & Sanders, A. A. Compartments within a compartment: what *C. elegans* can tell us about ciliary subdomain composition, biogenesis, function, and disease. *Organogenesis* **10**, 126–137 (2014).
- Hsiao, Y. C., Tuz, K. & Ferland, R. J. Trafficking in and to the primary cilium. *Cilia* **1**, 4 (2012).
- Chih, B. *et al.* A ciliopathy complex at the transition zone protects the cilia as a privileged membrane domain. *Nat. Cell Biol.* **14**, 61–72 (2011).
- Craige, B. *et al.* CEP290 tethers flagellar transition zone microtubules to the membrane and regulates flagellar protein content. *J. Cell Biol.* **190**, 927–940 (2010).
- Garcia-Gonzalo, F. R. *et al.* A transition zone complex regulates mammalian ciliogenesis and ciliary membrane composition. *Nat. Genet.* **43**, 776–784 (2011).

8. Hu, Q. *et al.* A septin diffusion barrier at the base of the primary cilium maintains ciliary membrane protein distribution. *Science* **329**, 436–439 (2010).
9. Kee, H. L. *et al.* A size-exclusion permeability barrier and nucleoporins characterize a ciliary pore complex that regulates transport into cilia. *Nat. Cell Biol.* **14**, 431–437 (2012).
10. Williams, C. L. *et al.* MKS and NPHP modules cooperate to establish basal body/transition zone membrane associations and ciliary gate function during ciliogenesis. *J. Cell Biol.* **192**, 1023–1041 (2011).
11. Gilula, N. B. & Satir, P. The ciliary necklace. A ciliary membrane specialization. *J. Cell Biol.* **53**, 494–509 (1972).
12. Heller, R. F. & Gordon, R. E. Chronic effects of nitrogen dioxide on cilia in hamster bronchioles. *Exp. Lung Res.* **10**, 137–152 (1986).
13. Roberson, E. C. *et al.* TMEM231, mutated in orofacioidigital and Meckel syndromes, organizes the ciliary transition zone. *J. Cell Biol.* **209**, 129–142 (2015).
14. Cevik, S. *et al.* Active transport and diffusion barriers restrict Joubert syndrome-associated ARL13B/ARL-13 to an Inv-like ciliary membrane subdomain. *PLoS Genet.* **9**, e1003977 (2013).
15. Huang, L. *et al.* TMEM237 is mutated in individuals with a Joubert syndrome related disorder and expands the role of the TMEM family at the ciliary transition zone. *Am. J. Hum. Genet.* **89**, 713–730 (2011).
16. Jauregui, A. R., Nguyen, K. C., Hall, D. H. & Barr, M. M. The *Caenorhabditis elegans* nephrocystins act as global modifiers of cilium structure. *J. Cell Biol.* **180**, 973–988 (2008).
17. Williams, C. L., Winkelbauer, M. E., Schafer, J. C., Michaud, E. J. & Yoder, B. K. Functional redundancy of the B9 proteins and nephrocystins in *Caenorhabditis elegans* ciliogenesis. *Mol. Biol. Cell* **19**, 2154–2168 (2008).
18. Schouteden, C., Serwas, D., Palfy, M. & Dammermann, A. The ciliary transition zone functions in cell adhesion but is dispensable for axoneme assembly in *C. elegans*. *J. Cell Biol.* **210**, 35–44 (2015).
19. Jensen, V. L. *et al.* Formation of the transition zone by Mks5/Rpgr1L establishes a ciliary zone of exclusion (CIZE) that compartmentalises ciliary signalling proteins and controls PIP2 ciliary abundance. *EMBO J.* **34**, 2537–2556 (2015).
20. Baughman, J. M. *et al.* A computational screen for regulators of oxidative phosphorylation implicates SLIRP in mitochondrial RNA homeostasis. *PLoS Genet.* **5**, e1000590 (2009).
21. van Dam, T. J., Wheway, G., Slaats, G. G., Huynen, M. A. & Giles, R. H. The SYSCILIA gold standard (SCGSv1) of known ciliary components and its applications within a systems biology consortium. *Cilia* **2**, 7 (2013).
22. Barker, A. R., Renzaglia, K. S., Fry, K. & Dawe, H. R. Bioinformatic analysis of ciliary transition zone proteins reveals insights into the evolution of ciliopathy networks. *BMC Genomics* **15**, 531 (2014).
23. Christopher, K. J., Wang, B., Kong, Y. & Weatherbee, S. D. Forward genetics uncovers Transmembrane protein 107 as a novel factor required for ciliogenesis and Sonic hedgehog signaling. *Dev. Biol.* **368**, 382–392 (2012).
24. Giles, R. H., Ajzenberg, H. & Jackson, P. K. 3D spheroid model of mIMCD3 cells for studying ciliopathies and renal epithelial disorders. *Nat. Protoc.* **9**, 2725–2731 (2014).
25. Friedland, A. E. *et al.* Heritable genome editing in *C. elegans* via a CRISPR-Cas9 system. *Nat. Methods* **10**, 741–743 (2013).
26. Starich, T. A. *et al.* Mutations affecting the chemosensory neurons of *Caenorhabditis elegans*. *Genetics* **139**, 171–188 (1995).
27. Williams, C. L., Masyukova, S. V. & Yoder, B. K. Normal ciliogenesis requires synergy between the cystic kidney disease genes MKS-3 and NPHP-4. *J. Am. Soc. Nephrol.* **21**, 782–793 (2010).
28. Valente, E. M. *et al.* Mutations in TMEM216 perturb ciliogenesis and cause Joubert, Meckel and related syndromes. *Nat. Genet.* **42**, 619–625 (2010).
29. Kensche, P. R., van Noort, V., Dutilh, B. E. & Huynen, M. A. Practical and theoretical advances in predicting the function of a protein by its phylogenetic distribution. *J. R. Soc.* **5**, 151–170 (2008).
30. Iglesias, A. *et al.* The usefulness of whole-exome sequencing in routine clinical practice. *Genet. Med.* **16**, 922–931 (2014).
31. Shaheen, R. *et al.* Identification of a novel MKS locus defined by TMEM107 mutation. *Hum. Mol. Genet.* **24**, 5211–5218 (2015).
32. Nakada, C. *et al.* Accumulation of anchored proteins forms membrane diffusion barriers during neuronal polarization. *Nat. Cell Biol.* **5**, 626–632 (2003).
33. Xu, K., Zhong, G. & Zhuang, X. Actin, spectrin, and associated proteins form a periodic cytoskeletal structure in axons. *Science* **339**, 452–456 (2013).
34. van Dam, T. J. *et al.* Evolution of modular intraflagellar transport from a coatomer-like progenitor. *Proc. Natl Acad. Sci. USA* **110**, 6943–6948 (2013).

## METHODS

**Coexpression analyses.** We collected a set of 20 genes known to localize at the TZ (ref. 1). Nucleoporins were excluded because they have an additional role in nuclear transport and are therefore likely to have substantially different expression profiles compared with other TZ proteins. The SYSCILIA gold standard (SCGSv1; <http://www.syscilia.org/goldstandard.shtml>)<sup>21</sup> was used to evaluate the approach for retrieving cilia-related genes. A large collection of publicly available microarray data sets was obtained from the NCBI gene expression omnibus (GEO) database: 809 data sets for mouse (~13,000 individual experiments) and 868 data sets for human (~22,000 individual experiments); the full list of the human and mouse GEO (microarray) data sets (GDS) employed is shown in Supplementary Table 2. Each expression data set was assessed for its potential to find new TZ-related genes by determining the expression coherence of the 20 genes known to localize to the TZ. Experiments where known TZ genes show coherent expression obtain a high weighting, and contribute more to the coexpression calculation than experiments with less coherent expression. These weightings are used to calculate an integrated probability for each gene, according to how much its expression profile correlates with that of TZ genes across the expression data sets. We calculated TZ coexpression separately for mouse and human, obtaining scores for ~15,000 mouse genes and ~21,000 human genes.

**Sequence analysis and evolutionary analysis.** Worm and human MKS and NPHP module protein sequences were extracted from NCBI. Orthologous sequences were detected by BLAST and PSI-BLAST and extracted from an in-house protein sequence and orthology database<sup>34</sup>. Retrieved sequences were manually verified by reverse BLAST searches. Hidden Markov Models (HMMs) were created for each protein family by first aligning the sequence using MAFFT (version v6.884b, options *-localpair -maxiterate 1000*). Highly fragmented sequences were removed from the alignment. Custom HMMs were created using HMMer 3.0 and searched against our in-house protein sequence database again for sequences missed by PSI-BLAST. Finally we searched the genomic and EST sequences using TBLASTN to find orthologues not found by gene prediction algorithms. For MKS-5 (RPGRIP1L), we also employed sequential sequence searches using NCBI PSI-BLAST using stepwise more diverse orthologous sequences as the seed (for example, we used the *Phytophthora infestans* sequence to find the *Chlamydomonas reinhardtii* sequence and used that sequence to find the *Volvox carterii* orthologue). Discovered sequences were confirmed by reverse PSI-BLAST searches and sequence alignments. All presences and absences were noted for each species considered (Supplementary Fig. 1). The TMEM107 alignment was made using MAFFT (options *-globalpair -maxiterate 1000*) and edited to fix minor alignment errors. For the differential Dollo parsimony (diff Dollop)<sup>29</sup> analysis, which counts the number of independent losses of proteins along a phylogenetic tree, we used a script provided by P. Kensch<sup>29</sup>. The network was constructed and visualized in Cytoscape.

**Targeted next-generation and exome sequencing analysis.** Next-generation sequencing analyses were performed on 5 µg of DNA sample from each of 198 JBTS and OFD individuals. In 192 JBTS individuals, simultaneous target sequencing was performed using a panel of 25 candidate or causal JBTS genes on an Illumina MiSeq in accordance with the manufacturer's recommendations. In 6 OFD individuals, exome capture was achieved using the SureSelect Human All Exon 50Mb kit (Agilent). The resulting libraries underwent 2 × 100-bp paired-end sequencing on an Illumina HiSeq 2000 in accordance with the manufacturer's recommendations. Reads were aligned to the human reference genome (GRCh37/hg19) with the Burrows-Wheeler Aligner (BWA.0.5.6) and potential duplicate paired-end reads were removed using picardtools.1.22 (<http://picard.sourceforge.net>). The Genome Analysis Toolkit (GATK) 1.0.57 was used for base quality score recalibration and indel realignment, as well as for single-nucleotide variant and indel discovery and genotyping using standard hard filtering parameters. Homozygous variants with quality scores of >30, sequencing depth of >4, quality/depth ratio of >5.0 and strand bias of <-0.10 were retained for subsequent analyses. Coverage was assessed with the GATK Depth of Coverage tool by ignoring reads with mapping quality of <20 and bases with base quality of <30. Candidate events were inspected using Integrative Genomics Viewer (IGV). Variants were excluded when the frequency was >1/1,000 in the Exome Variant Server, NHLBI (<http://evs.gs.washington.edu/EVS>). The sequencing data have been deposited in the European Nucleotide Archive (<http://www.ebi.ac.uk/ena>); accession number PRJEB11176.

**Sanger sequencing.** TMEM107 (NM\_183065) mutation screening was performed by direct sequencing of PCR products (coding exons and adjacent intronic junctions) in 40 additional JBTS individuals, 54 MKS patients (mutation-negative for known genes), and 32 other patients with a clinical diagnosis consistent with a ciliopathy. PCR primers (sequences available on request) were designed with Primer3 (<http://bioinfo.ut.ee/primer3-0.4.0/primer3>). PCR products were purified using the Exo-SAP cleanup kit (USB). Sequencing was performed using the ABI

BigDye Terminator Cycle Sequencing kit (v3.1; Applied Biosystems) following the manufacturer's instructions in an ABI 3130 sequencer 7 (Applied Biosystems). Sequence data were analysed with SeqScape v2.7 (Applied Biosystems). The impact of the missense mutation was assessed using PolyPhen-2 (<http://genetics.bwh.harvard.edu/pph2>). Written consent was obtained from patients for generation and use of their molecular data.

**C. elegans strains, maintenance and crossing.** *C. elegans* were maintained and cultured at 20 °C using standard techniques. All strains employed are shown in Supplementary Table 4. Standard genetic crossing techniques were used to make double mutants and to introduce transgenes into genetic backgrounds. Genotyping was performed using PCR (primer sequences available on request). The *daf-19(m86)* mutation was followed using the dye-filling assay<sup>35</sup>.

**Generation of the *oq100* mutation by CRISPR.** sgRNA template and Cas9 plasmids were obtained from Addgene (46168, 46169). The *tmem-107*-sgRNA was generated following ref. 25, targeting the sequence 5'-ATAGAGATCGAGACGGCGAC-3'. sgRNA and Cas9 constructs were each injected at 125 ng µl<sup>-1</sup>, together with the pCeh361 (*dpy-5(+)*) construct at 50 ng µl<sup>-1</sup>, into *dpy-5(e907)* hermaphrodites. A total of 204 *dpy-5* rescued F1 worms were screened for a *tmem-107*-associated Hpy99I (NEB R0615) restriction fragment length polymorphism (RFLP). Three independent lines with an RFLP were subjected to Sanger sequencing to identify the *tmem-107* mutations. Two worms had the same in-frame 6-bp deletion (P74S75del), predicted to cause no serious effects and were not investigated further. The third worm possessed a 27-bp deletion in exon 2 (genomic breakpoints: 1:14758954/14758955–14758981/14758982) replaced with a 14-bp insertion (5'-GTGACAACGTGGAA-3'). This allele designated *oq100* features a frameshift leading to a predicted truncated protein of 72 native amino acids followed by an ectopic 17 amino acids and a premature stop.

**C. elegans reporters.** All constructs were generated by fusion PCR as previously described<sup>36</sup>. For the transcriptional (promoter) *tmem-107p::GFP* reporter, GFP amplified from pPD95.67 was fused with 559 bp of *tmem-107*'s 5'UTR sequence along with the first 15 bp of exon 1 (with the adenine of the start codon mutated to cytosine). For the translational (protein) *tmem-107::gfp* reporter, the entire exonic and intronic sequence of each gene, together with upstream promoter sequence (see above), was fused in-frame with GFP amplified from pPD95.77. For substituting extramembranous TMEM-107 sequences Polyphobius software (<http://phobius.sbc.su.se/poly.html>) was employed to determine TMEM-107 residue topology twice: based on *C. elegans* only; and based on sequence conservation in *C. elegans* close relatives. Subsequently, a consensus prediction was compiled, establishing that amino acids 1–9 (N terminus), 30–47 (linker 1), 73–78 (linker 2) and 100–103 (linker 3) are very likely extramembranous. Next, we searched the literature for tetraspan transmembrane proteins not associated with ciliary TZs and identified with the software Phobius (<http://phobius.sbc.su.se>) similar sized linker sequences, suitable for replacing TMEM107 linkers; amino acids 131–148 of SNG-1 to substitute linker 1, amino acids 74–79 of SPE-38 to replace linker 2, and amino acids 49–52 to substitute linker 3. In addition, we generated three constructs replacing the TMEM-107 linkers (1–3) with sequences containing scrambled versions of the same residues. The TMEM-107 C-terminal truncation construct TMEM-107(aa1–129)::GFP—called cTMEM107 in Fig. 4c—was similarly amplified except that the C-terminal 7 amino acid encoding sequence was not included. The TMEM-107 N-terminal substituted construct (SPH-1(aa1–11)::TMEM-107 (10–136)::GFP)—called nTMEM-107 in Fig. 4c—was amplified to contain the N-terminal 11 amino acids of SPH-1 fused to TMEM-107 lacking its N terminus. The SPH-1 N terminus was chosen as the replacement because SPH-1 and TMEM-107 are topologically similar; both are predicted tetraspan transmembrane proteins with cytosolic N-terminal tails (albeit of different sequence). Note that full-length SPH-1::GFP, SNG-1::GFP and SPE-38::GFP translational reporters (under the control of an *arl-13* promoter active in most ciliated cells) do not localize to ciliary TZs (data not shown). For mimicking the TMEM-107 patient variants, PCR was used to engineer E46G (equivalent to human HsE45G) and F96del (equivalent to HsF106del) mutations into nematode TMEM-107. For simulating the HsL134Ffs\*8 mutation, TMEM-107 was truncated at L120, and nucleotides corresponding to the human ectopic residues (FSSPSLG) were added. Transgenic worms expressing the above constructs were generated using gonadal transformation through microinjection. The transcriptional construct was injected into *dpy-5(e907)* worms at 50 ng µl<sup>-1</sup>, together with the *dpy-5(+)*-containing rescuing construct (at 50 ng µl<sup>-1</sup>), pCeh361. Translational constructs were injected into N2 worms typically at 5 ng µl<sup>-1</sup>, together with a coelomocyte cell-expressed (*unc-122p::gfp* or *unc-122p::dsRed*) co-injection marker at 100 ng µl<sup>-1</sup>.

**C. elegans immobilization for microscopy.** Live worms were immobilized on 10% agarose pads using microbeads (Polysciences no. 00876-15) or with 40 mM tetramisole (Sigma no. L9756).

**C. elegans fluorescence imaging and FRAP assay.** Imaging was performed on an epifluorescence-fitted upright Leica DM5000B compound microscope or an inverted Nikon Eclipse Ti microscope with a Yokogawa spinning-disc unit (Andor Revolution). Image analysis and formatting was conducted using ImageJ software (NIH). Fluorescence recovery after photobleaching (FRAP) assays were performed using the above confocal system, with an attached FRAPPA unit. Samples were imaged pre-bleach, and then bleached using a single pulse of the 488 nm laser at 100% with a dwell time of 100  $\mu$ s. Images were recorded immediately post-bleach (that is, 0 minute time point) and at varying time points post-bleach until recovery plateaued. All images were taken using the same camera settings (exposure time, gain) and images were subsequently stacked to ensure identical background intensities. Using ImageJ, photobleached and non-photobleached regions were selected and the intensity (grey value) was measured at each time point. After background subtraction, ratios of bleached/non-bleached regions were calculated, and ratios were normalized to a pre-bleach ratio of 1.0.

**Dye-filling, chemosensory and roaming (foraging) assays.** Assays for dye-filling (Dil), roaming and chemoattraction to a volatile odorant (isoamyl alcohol) were performed as previously described<sup>35</sup>. A chemotaxis index was calculated at 30 min and 60 min. For the roaming assay, single worms were placed for 16 h onto seeded plates and track coverage was assessed using a grid reference.

**Transmission electron microscopy.** Young adult worms were fixed, sectioned and imaged using previously reported methodology<sup>35</sup>. For the TEM electron tomography, 200-nm-thick sections were collected onto Formvar carbon-coated slot grids and a tilt series acquired from  $-60$  to  $+60$  in  $1^\circ$  increments using FEI software. The tilt series was converted to a  $z$  stack using serial EM and then visualized using Amira software (FEI).

**Cloning of mammalian constructs.** Full-length *TMEM107* was cloned into the pcDNA3.0 vector (Invitrogen), and then shuttled into mCherry-, EGFP-, and FLAG- containing vectors. Mutations were introduced into *TMEM107*-pEGFP-N3 by QuickChange mutagenesis (Stratagene).

**Immortalized mammalian cell lines and antibodies.** Mouse inner medullary collecting duct (IMCD3), human retinal pigmented epithelial (hTERT-RPE1) and human embryonic kidney (HEK293) cells were derived from the American Type Culture Collection (ATCC). The genomic status was assessed by array CGH and karyotyping (May 2013) and tested every three months for mycoplasma. Cells were maintained in DMEM/Ham's F12 medium supplemented with 10% fetal calf serum (FCS), under standard conditions (37°C, 5% CO<sub>2</sub>) at low passages (<25). Human renal proximal epithelial cells (RPTEC-TERT1) were provided by T. McMorro (University College Dublin). Three-dimensional spheroids (IMCD3 cells) were grown and scored as previously described<sup>24</sup>. Primary antibodies: mouse monoclonal anti-denatured GFP (Sigma-Aldrich cat. no. G6539, clone GFP-20), rabbit polyclonal anti-native GFP (A.V. peptide, 'Living Colors', Clontech cat. no. 632377), mouse anti- $\gamma$ -tubulin, mouse anti-acetylated-tubulin (Sigma-Aldrich cat. no. T7451, clone 6-11B-1), rabbit anti- $\gamma$ -tubulin and mouse anti- $\beta$  actin (Abcam cat. no. ab6276, clone AC-15). Guinea pig anti-RPGRIP1L (ref. 37), rabbit anti-TMEM237 (ref. 15), and rabbit anti-TMEM231 (ref. 5) have been previously described. Secondary antibodies: polyclonal Alexa Fluor 488-, Alexa Fluor 594- and Alexa Fluor 568-conjugated goat anti-mouse IgG, and goat anti-rabbit IgG (Molecular Probes; cat. no. A-11001/A-11005/A-11031/A-110034).

**Ciliogenesis assays with human primary fibroblast cells.** Patient fibroblasts were stored in the CRB Ferdinand Cabanne Biobank (Dijon). Fibroblasts were grown from skin biopsies in DMEM supplemented with 10% FCS and 1% P/S. Cells were incubated at 37°C in 5% CO<sub>2</sub> to approximately 90% confluence. Fibroblasts were serum starved for 24 h before fixation with 4% PFA for 5 min at room temperature followed by ice-cold methanol for 3 min and blocked in PBS (containing 1% BSA and 0.1% Triton X-100) for 30 min. Fixed cells were incubated in primary antibodies diluted in block solution (mouse anti-acetylated tubulin; Sigma T6793; 1:10,000, rabbit anti-ARL13b; ProteinTech 17711-1-AP; 1:400) for 90 min at room temperature and Alexa Fluor-conjugated secondary antibodies from Life Technologies (donkey anti-rabbit 568; 1:400, donkey anti-mouse 647; 1:400) and Hoechst333 for 60 min at room temperature. Coverslips were mounted using Fluoromount G. Confocal imaging was performed using a Zeiss LSM700. Approximately 70 events per condition were scored. GraphPad Prism 5.0 was used to perform two-tailed Student's  $t$ -tests.

**Immunofluorescence assays with *Tmem107*-depleted IMCD3 cells.** For co-localization assays (Fig. 4d), murine IMCD3 cells were seeded at  $2.5 \times 10^5$  (ref. 5) cells per well on sterile glass coverslips in six-well plates. Lipofectamine RNAiMAX (LifeTechnologies) was used to transfect cells with the siRNA SMARTpool targeting

*Tmem107* (Dharmacon) according to the manufacturer's protocol. After 72 h, cells were fixed in ice-cold methanol, blocked in 1% non-fat milk and processed for immunofluorescence microscopy via standard methods<sup>38</sup> using Alexa Fluor 488- or Alexa Fluor 568-conjugated secondary antibodies (1:500, LifeTechnologies). Confocal images were obtained using a Nikon A1R confocal microscope with a  $\times 100$  oil objective lens controlled by NIS-Elements AR 4.20.01 (Nikon) software. Optical sections were generated through structured processing using AxioVision 4.3 (Zeiss) or NIS-Elements AR 4.20.01 (Nikon) software. Co-localization analyses were performed using the FIJI software plug-in 'Co-localization Threshold'. For knockdown experiments in Fig. 2a,b, murine IMCD3 cells were transfected with a siRNA SMARTpool targeting *Tmem107* (Dharmacon), and spheroids were grown and scored as previously described<sup>24</sup>.

**Co-immunoprecipitation assays.** For transfection with plasmids, cells at 90% confluency were transfected using Lipofectamine 2000 (Invitrogen) according to the manufacturer's instructions. Cells were incubated for 24 to 72 h before lysis or immunostaining. Co-immunoprecipitation was performed as described previously, except that 10 mM CHAPS was used as zwitterionic detergent in the lysis buffer<sup>28</sup>. Whole-cell extracts (WCEs) were prepared from confluent IMCD3 cells transiently transfected with 1.0  $\mu$ g plasmid constructs in 90 mm tissue culture dishes, or scaled down as appropriate. WCE supernatants were processed for immunoprecipitation experiments by using 5  $\mu$ g affinity-purified mouse anti-GFP ('Living Colors', Clontech), or 5  $\mu$ g monoclonal antibodies, or 5–10  $\mu$ g purified IgG fractions from rabbit polyclonal antisera, coupled to protein G- and/or protein A-Sepharose beads (GE Healthcare). The affinity-purified rabbit polyclonal anti-TMEM17 and TMEM231 have been described previously<sup>5</sup>. Immunoprecipitations were performed in reduced-salt incubation buffer (20 mM Tris, pH 7.5, 25 mM NaCl, 2 mM EDTA, 0.5 mM EGTA, 0.02% (w/v) Na<sub>3</sub>S, 10% (v/v) glycerol, 10% (v/v) ethanol, 0.1% (v/v) protease inhibitor cocktail) containing 1 mM CHAPS. Proteins were analysed by SDS-PAGE (using 4–12% polyacrylamide gradient gels) and western immunoblotting according to standard protocols using either rabbit polyclonal antisera (final dilutions of 1:200–1000) or monoclonal antibodies (1:1,000–5,000). Appropriate HRP-conjugated secondary antibodies (Dako) were used (final dilutions of 1:10,000–25,000) for detection by the enhanced chemiluminescence 'Femto West' western blotting detection system (Pierce).

**Stimulated emission depletion (STED) microscopy.** STED imaging was performed on a Leica DMI6000 SP8X CW gated STED system with a 592 nm depletion laser and an HCX PL APO  $\times 100$  NA1.40 oil objective. Samples were excited at 488 nm and emission was detected between 510 and 540 nm. Pixel size was <20 nm (typically  $\sim 15$  nm). Images were deconvolved using Huygens Professional software (Scientific Volume Imaging B.V), which is part of the standard configuration of the Leica STED system. For deconvolution a signal to noise ratio of 7 was employed and the 'classic' algorithm selected. All other parameters used were default values (contained in the meta data for each image file), as defined by the Huygens's deconvolution wizard.

**Mammalian cell preparation for STED microscopy.** RPTEC-TERT1 cells were seeded on glass coverslips and cultured for at least 7 days on reaching confluence to induce primary cilia formation. Cells were fixed with 3% PFA for 5 min at room temperature followed by ice-cold methanol for 5 min. After blocking with 3% BSA in 0.2% Triton X-100/PBS for 30 min, cells were stained for TZ proteins (guinea pig anti-RPGRIP1L, 1:500, or rabbit anti-TMEM67, 1:200) and the ciliary axoneme (mouse anti-polyglutamylated tubulin, 1:1,000; Adipogen; cat. no. AG-20B-0020-C100; clone GT335) at room temperature for 2 h. Primary antibodies were detected with polyclonal Alexa Fluor-conjugated secondary antibodies (1:100 dilution; 1 h at room temperature); goat anti-guinea pig 488 (Molecular Probes; cat. no. A11073), goat anti-rabbit 488 (Molecular Probes; cat. no. A11008) or goat anti-mouse 568. All antibodies were diluted in blocking solution. Coverslips were mounted on glass slides in ProLong Diamond (Life Technologies).

**Direct stochastic optical reconstruction microscopy (STORM) system.** The dSTORM system was based on the 3D PALM system in ref. 39. We used an inverted microscope (Olympus, IX81 with additional side-port ILL100-TIRZD) fitted with an automated  $x$ - $y$  stage with additional piezoelectric adjustment in  $z$  (Applied Scientific Instrumentation, PZ-2000). The objective lens was a  $\times 60$ , 1.2 NA, water immersion lens (Olympus, UPLSAPO60XW). The system included a focus locking device that reduced  $z$ -drift during calibration and data acquisition (Mad City Labs, C-focus) and a cylindrical lens (Thorlabs,  $f = 100$  mm, LJ1567RM-A). Images were captured by a back-thinned, electron-multiplying CCD (charge-coupled device) camera, cooled to  $-80^\circ\text{C}$  (Andor Technology, iXON Ultra, model DU-897U-CSO-#BV), using published scripts called from the camera interface (Andor Technology, SOLIS). This also converted SIF images generated by the camera to DAT format for processing.

**Preparation of secondary antibody and samples for dSTORM.** Affinity-purified guinea pig anti-RPGRIP1L has been described previously<sup>37</sup>, and was used at 1:200 dilution. Polyclonal donkey anti-guinea pig IgG (H+L) secondary antibody (100 µg) was labelled ('AffiniPure', Jackson ImmunoResearch Europe cat. no. 706-005-148) in PBS containing 120 mM NaHCO<sub>3</sub> with 2 µg carboxylic acid succinimidyl ester of the photoswitchable dye Alexa Fluor 647 (A37573, Life Technologies). Labelling was performed for 30 min at room temperature, and unincorporated dye was removed by gel filtration through NAP-5 columns (17-0853-02, GE Healthcare) according to the manufacturer's protocol. Antibody/dye labelling ratios of approximately 1:1 were confirmed by measured absorbances in a spectrophotometer, with a final concentration of 0.3 µg µl<sup>-1</sup>. Secondary antibodies were used at titres of 1:100.

Human hTERT-RPE1 cells were seeded on cleaned coverslips (no. 1.5, 25-mm diameter CS-25R15; Warner Instruments) at 2.5 × 10 (ref. 5) cells per well on the coverslips in six-well plates and serum starved in normal media with 0.2% FCS for 48 h to induce ciliogenesis. Coverslips were processed for immunofluorescence staining using standard methods, and post-fixed with 3% paraformaldehyde/0.1% glutaraldehyde in PBS. Coverslips were then incubated with 0.01% poly-L-lysine (Sigma-Aldrich, P4707) for 10 min followed by a suspension of 100 nm gold nanoparticles (1:10, Sigma-Aldrich 724031, in PBS) for use as fiducials. Calibration series for depth information (see below) were taken at this point, using the relevant excitation laser(s). Data were acquired in the presence of fluorescence quenching buffer consisting of 10 mM Tris-HCl (pH 8.0), 50 mM NaCl, 5 mg ml<sup>-1</sup> glucose, 114 mM β-mercaptoethanol, 0.5 mg ml<sup>-1</sup> glucose oxidase and 40 µg ml<sup>-1</sup> catalase.

**dSTORM image acquisition, processing and analysis.** Imaging software employed was described previously<sup>39</sup> (see <https://github.com/AndrewGYork/palm3d> for further details). Calibration images were taken to calculate the point spread function (PSF) in steps of 50 nm over a 4 µm range, using fluorescence of selected fiducials. Labels were then excited until emission was quenched and then stochastically re-activated using a 405 nm laser initially at low power (0.4 mW), followed by data collection. Fluorescence emission events were localized in *x-y* and *z* using the PSFs captured in the calibration series<sup>39</sup>. Drift was recorded and corrected using images of the fiducials. Emission events

were binned into a histogram for display and to correct for distortion by the cylindrical lens. Binning was at either 20 nm or 10 nm, with *x-y-z* localization precisions of 20 × 30 × 50 nm for fiducial markers<sup>39</sup>. The software applied smoothing to reflect the limits of localization precision, and *z*-stacks were displayed in FIJI.

**Statement of image representation and reproducibility.** Representative images are shown for all worm and mammalian cell imaging. The following states how many samples were imaged in each figure panel where a representative image is shown: Fig. 1c,d (>30 worms), Fig. 1e (30 cells), Fig. 2b (50 spheroids), Fig. 2h (75 cells), Fig. 3b (>20 worms for each strain), Fig. 3c (>50 worms for each strain), Fig. 3d (>20 worms for each strain), Fig. 3f (>30 worms for each strain), Fig. 3g (>50 worms for each strain), Fig. 3h (>30 worms for each strain), Fig. 4a (>40 worms for each strain), Fig. 4c (>20 worms for each strain), Fig. 4d (50 cells for each experiment), Fig. 5a (>20 worms for each strain), Fig. 5b (10 worms), Fig. 5c (>100 worms imaged per strain), 5d (>30 cells per experiment), Fig. 5e (>20 TZs for each marker), Supplementary Fig. 2a (>20 worms), Supplementary Fig. 2b (>40 worms), Supplementary Fig. 2d (>20 worms), Supplementary Fig. 2e (>30 cells), Supplementary Fig. 4a (2–4 amphid pores), Supplementary Fig. 4b (>20 transition zones), Supplementary Fig. 4c (>30 worms per strain), Supplementary Fig. 5a (>10 sets of amphid transition zones).

35. Sanders, A. A., Kennedy, J. & Blacque, O. E. Image analysis of *Caenorhabditis elegans* ciliary transition zone structure, ultrastructure, molecular composition, and function. *Methods Cell Biol.* **127**, 323–347 (2015).
36. Hobert, O. PCR fusion-based approach to create reporter gene constructs for expression analysis in transgenic *C. elegans*. *BioTechniques* **32**, 728–730 (2002).
37. Arts, H. H. *et al.* Mutations in the gene encoding the basal body protein RPGRIP1L, a nephrocystin-4 interactor, cause Joubert syndrome. *Nat. Genet.* **39**, 882–888 (2007).
38. Dawe, H. R. *et al.* Nesprin-2 interacts with meckelin and mediates ciliogenesis via remodelling of the actin cytoskeleton. *J. Cell Sci.* **122**, 2716–2726 (2009).
39. York, A. G., Ghitani, A., Vaziri, A., Davidson, M. W. & Shroff, H. Confined activation and subdiffraction localization enables whole-cell PALM with genetically expressed probes. *Nat. Methods* **8**, 327–333 (2011).